THE JOURNAL OF PHYSICAL CHEMISTRY C

Article

pubs.acs.org/JPCC

Electronic and Geometric Structure of Ce^{3+} Forming Under Reducing Conditions in Shaped Ceria Nanoparticles Promoted by Platinum

O. V. Safonova,*[,†] A. A. Guda,[‡] C. Paun,[§] N. Smolentsev,[‡] P. M. Abdala,[∥] G. Smolentsev,[†] M. Nachtegaal,[†] J. Szlachetko,[†] M. A. Soldatov,[‡] A. V. Soldatov,[‡] and J. A. van Bokhoven*[,†,§]

[†]Paul Scherrer Institut, 5232 Villigen, Switzerland

[‡]Research Center for Nanoscale Structure of Matter, Southern Federal University, 344090 Rostov-on-Don, Russia

[§]ETH Zurich, Institute for Chemical and Bioengineering, 8093 Zurich, Switzerland

[∥]SNBL at ESRF, 38043 Grenoble, France

Supporting Information

ABSTRACT: The structure of Ce^{3+}, which is responsible for the low-temperature oxygen storage capacity of ceria, was determined by high-energy-resolution fluorescence detected X-ray absorption spectroscopy at the Ce L_3 and L_1 edges. Well-defined ceria nanoparticles (rods, truncated octahedra, and cubes) were synthesized hydrothermally and promoted by platinum nanoparticles. The electronic structure of Ce^{3+} does not depend significantly on the nature of the exposed crystallographic planes of CeO_2 particles; it does, however, differ from the electronic structure of known stable compounds containing Ce^{3+} ions, such as $CeAlO_3$, $Ce(NO_3)_3{\cdot}6H_2O$, and $Ce_2Zr_2O_7$. Theoretical simulation of Ce L_1 and L_3 X-ray absorption spectra, quantitative analysis of the oxygen storage capacity, and X-ray diffraction data suggest that Ce^{3+} ions form both at the surface and in the near-surface layer. Surface and bulk Ce^{3+} ions are characterized by elongated Ce−O distances in the first coordination shell and almost the same Ce−Ce distances in the second coordination shell with respect to Ce^{4+} in stoichiometric CeO_2. Ce^{3+} ions on the surface of the nanoparticles surface may have a smaller number of oxygen neighbors (as low as six), while in the near-surface layer they tend to have an 8-fold coordination, thus producing oxygen deficit structures similar to $Ce_{11}O_{20}$.

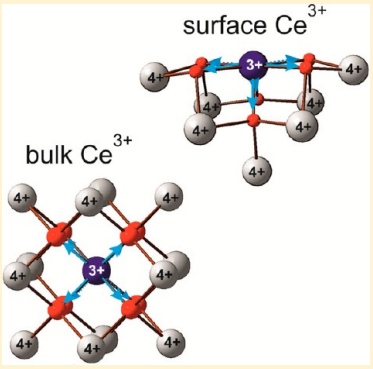

1. INTRODUCTION

Nanocrystalline ceria finds application as an active component in three-way catalysts and catalytic material for the oxidation of CO, hydrocarbons, and soot.[1,2] Combining ionic conductivity with catalytic properties, ceria-based ceramics are promising candidates for the development of high-temperature fuel cells[3,4] and for the solar-driven thermochemical dissociation of CO_2 and H_2O.[5]

The most important feature of ceria in all these applications is its ability to store and release oxygen, the amount of which is characterized by the oxygen storage capacity (OSC).[1] OSC is defined as the reversible release of oxygen from a material structure; the released oxygen catalyzes chemical reactions at low concentrations of an oxidizing agent in the feed. Release of oxygen from ceria is accompanied by the formation of oxygen vacancies and Ce^{3+} ions. Two types of OSC can be distinguished. High temperature OSC takes place above 500 °C. The oxygen atoms from deep layers of the CeO_2 structure participate in chemical reactions, which can result in the formation of oxygen deficit phases such as $CeO_{1.68}$, $Ce_{11}O_{20}$, or Ce_7O_{12}.[6] Low temperature (LT) OSC occurs below 500 °C and is particularly important in catalytic applications. In this case the total amount of oxygen atoms that can be extracted from the CeO_2 structure does not exceed 0.5−2 surface monolayers.[7,8] LT OSC is higher for ceria nanoparticles than for bulk crystals and is higher for the nanoparticles preferentially exposing (100) and (110) planes compared to nanoparticles with exposed (111) planes.[7] Noble and transition metals such as Pt, Pd, Rh, Au, Cu, and Ni facilitate the release of oxygen from ceria, thus enabling the observation of the LT OSC of ceria, even at room temperature.[1] However, the mechanism of LT OSC and the related structure of the reduced ceria surface on the atomic scale remain unknown. Several theoretical studies described the formation of oxygen vacancies and the local structure of Ce^{3+} sites in pure and Pt-promoted ceria nanoparticles and single crystal surfaces.[9−12] These studies suggest the formation of Ce^{3+} sites with a different local coordination in the first coordination shell, ranging from 4-fold coordination in fully reduced $CeO_2(111)$[10] to 8-fold coordination,[11] as well as showing either shortening[10] or elongation[11,13] of the Ce−O distances compared to stoichiometric CeO_2. Experimentally it is difficult to reveal the detailed local structure of Ce^{3+} in ceria. X-ray diffraction (XRD) is suitable only for the average structure, and even element-specific methods, such as

Received: September 25, 2013
Revised: January 6, 2014

   dx.doi.org/10.1021/jp409571b | J. Phys. Chem. C XXXX, XXX, XXX−XXX

extended X-ray absorption fines structure (EXAFS), cannot effectively probe the Ce−O coordination shell of Ce^{3+} with a majority of Ce^{4+} atoms in the structure. Kossoy et al.[14] studied the local structure of oxygen-deficit strained ceria films using a combination of XRD and EXAFS at the Ce L_3 edge. They observed elongation of the average Ce−O distance compared to stoichiometric CeO_2 by XRD and shortening of average Ce−O distance by EXAFS. These surprising results led to the conclusion that Ce−O_{vac} distances are longer than the average Ce−O distances in the CeO_{2-x} structure.

In the present work we probed the electronic and the geometric structure of Ce^{3+} and Ce^{4+} in ceria nanoparticles under reducing conditions by means of in situ high-energy-resolution fluorescence detected (HERFD) XANES spectroscopy at the Ce L_1 and L_3 edges combined with theoretical simulations. Several structural models of Ce^{3+} and Ce^{4+} in different local coordination on the surface and in the bulk structure of ceria nanoparticles were compared. The enhanced energy resolution of Ce L_3 HERFD XANES spectroscopy compared to traditional XANES spectroscopy and sensitivity to small changes in the electronic structure of cerium were demonstrated elsewhere.[15,16] However, Ce L_3 edge spectra are significantly affected by multielectron processes[17] and, therefore, are not considered to be an ideal for examining the geometric structure of cerium. In contrast, the Ce L_1 edge spectra affected to a much lesser extent by multielectronic processes and reveal more about the local structure of cerium. To obtain more in-depth information about the local and electronic structure of Ce^{3+} ions in ceria nanoparticles, we measured both absorption edges with enhanced energy resolution. The well-defined nanoparticles of ceria crystallized as truncated polyhedra, rods, and cubes were selected for this study. The results of the OSC measurements were quantitatively correlated with in situ Ce L_1 and L_3 HERFD XANES spectroscopy and lattice expansion monitored by XRD.

2. EXPERIMENTAL METHODS

Well-defined ceria nanoparticles, as rods (R), truncated octahedral (TO), and cubes (C), were prepared by a hydrothermal process according to published procedures;[7] the details are given in the Supporting Information (SI). The resulting powders were calcined in air at 500 °C for 6 h. The specific surface area of ceria was measured by nitrogen physisorption. Platinum nanoparticles were deposited on nanoceria by incipient wetness impregnation; the details are given in the SI. The concentration of platinum was 0.24 to 2 wt %, corresponding to surface densities of 0.18 to 1.0 at/nm^2. The samples were characterized by TEM using a Tecnai F30 ST (FEI) electron microscope with a field emission gun operated at 300 kV. The mean size of the platinum nanoparticles and the standard deviation were estimated based on 30 to 100 particles.

The total OSC of well-defined ceria-based nanomaterials was measured by means of a Catlab setup (Hiden Analytical) consisting of a plug-flow reactor and a quadrupole mass spectrometer (MS). Each sample (5−10 mg) was mixed with 20−25 mg of SiC and placed in a quartz tube (5 mm inner diameter) between two plugs of quartz wool. Before each experiment the samples were heated to 150 °C in an Ar flow and maintained in pure Ar for 3 h. At the same temperature, 40 pulses of 100 μL of 5% CO in He were introduced progressively into the reactor at intervals of 2 min using a VICI pulsing valve followed by 40 pulses of 2% O_2 in Ar at intervals of 1 min. The consumption of CO and O_2 in the respective pulses was calculated from the missing mass spectroscopic intensity in these pulses compared to the intensity after saturation. We repeated the series of CO and O_2 pulses three times and calculated the average OSC. We also measured OSC with pulses with different concentrations of CO and O_2 (1 and 5%) and found that the OSC does not depend on concentration of CO and O_2. This finding explains why the gas mixtures in our experiment contained slightly different concentrations of CO and O_2. To estimate the OSC related to oxidation and reduction of platinum nanoparticles, we measured the oxidation state of platinum in situ under oxidizing (4% O_2 in He) and reducing (5% CO in He) conditions by XANES at the Pt L_3 edge at 150 °C. The spectra were acquired at the SuperXAS beamline[18] of the Swiss Light Source (SLS, PSI, Villigen, Switzerland) using a Si(111) double-crystal monochromator, a Rh-coated collimating mirror at 2.8 mrad, and a Rh-coated focusing mirror. We used an in situ plug flow reactor[19] and an air blower heater to achieve the required experimental conditions. Pt foil and a pellet of a PtO_2 standard were measured in transmission mode and used as the references. Under oxidizing conditions after exposure to the oxygen pulses we expected that ceria is fully oxidized.[16] Under reducing conditions, after exposure to CO at 150 °C, the concentration of Ce^{3+} was twice that of oxygen vacancies. From the same experiments, we estimated the total number of oxygen layers lost by the ceria surface based on the theoretical density of oxygen on different crystallographic planes.[20] According to Mai et al.[7] we considered that truncated octahedra expose 50% of the (111) and 50% of the (100) planes, rods expose 50% of the (110) and 50% of the (100) planes, and cubes have only the (100) planes.

The in situ high-resolution XRD experiments were performed at the Swiss-Norwegian beamlines (SNBL)[18,19] at the European Synchrotron Radiation Facility (Grenoble, France) using a two-circle diffractometer equipped with six detectors and Si(111) analyzer crystals and NaI scintillation counters. The X-ray beam wavelength (λ) was set at 0.5 Å by a Si(111) channel-cut monochromator. The 2θ scan was acquired between 4 and 35° in steps of 0.005° for 60 min. The size of the X-ray beam in horizontal and vertical directions was 8 mm by 1.5 mm, respectively. The total beam intensity on the sample was about 5×10^{10} ph/s. The ceria powders were loaded into borosilicate glass capillaries (Hilgenberg) with 1 mm diameter and 0.01 mm thickness and fixed in the goniometer head, which was rotating with the constant speed during the data acquisition. To exclude possible damage induced by X-ray irradiation the position of Ce K-edge jump was checked for each sample before and after XRD experiment and no differences were observed. The XRD patterns under cycling in oxidizing (2% O_2 in He) and reducing (5% CO in He) atmospheres were measured in the above-mentioned in situ plug flow reactor.[19] The quantitative analysis of the XRD patterns was done according to the Rietveld method using the FullProf program package and the NPROF=7 profile function.[21] The wavelength and 2θ zero shift were precisely calibrated to a Si standard (SRM 2000, NIST).

The HERFD XANES spectra at the Ce L_1 and L_3 egdes were measured at the SuperXAS beamline at SLS (PSI, Villigen, Switzerland).[18] The incident photon beam was selected by a Si (111) double crystal monochromator, and the rejection of higher harmonics and focusing were achieved by a Si-coated collimating mirror at 2.8 mrad and a Rh-coated torroidal mirror

dx.doi.org/10.1021/jp409571b | J. Phys. Chem. C XXXX, XXX, XXX−XXX

Table 1. Structural Parameters of Reference Compounds and Model Structures: Formal Oxidation State and Bader Charge on Cerium, Description of First and Second Coordination Shells Including Number of Neighbors (N), Bond Length (R), and the Difference in the Bond Length ΔR Compared to CeO_2

		first shell (O)			second shell			
structure	oxidation state (Bader charge)	N	R, Å	ΔR, %	N	ΔR, Å	ΔR, %	ref
CeO_2	4+ (2.4)	8	2.34	0	12 Ce	3.83	0	37
$CeAlO_3$	3+ (2.1)	12	2.69	+15	8 Al	3.30	−14	38
$Ce(NO_3)_3 \cdot 6H_2O$	3+	11	2.65[a]	+13	3 N	3.15[a]	−18	39
$Ce_2Zr_2O_7$	3+ (2.2)	8	2.47[a]	+5.5	12 Zr	3.78[a]	−1.3	40
c-Ce_2O_3	3+ (2.1)	6	2.46[a]	+4.8	10 Ce	4.08[a]	+6.5	41
$Ce_{11}O_{20}$	3+ (2.1)	8	2.51[a]	+7	12 Ce	3.86[a]	+0.8	6
	4+ (2.4)	7	2.33[a]	−0.6	12 Ce	3.89[a]	+1.5	
CeO_2(111):Ce	3+ (2.0)	4	2.13 x1 2.27 x3	−4.7	9 Ce	3.90[a]	+1.8	10
Ce^{3+} in $Ce_{21}O_{41}$ (nano)	3+	6	2.25 x1 2.49 x5	+4.5	7 Ce	3.83[a]	0	11

[a]Average value.

at 2.8 mrad. The beamline was calibrated using a V foil (V K edge at 5465 eV). The size of the X-ray beam was 0.1 × 0.1 mm^2 with a total beam intensity of about 4×10^{11} ph/s. To measure Ce L_1 and L_3 HERFD XANES, spherically bent (R = 1000 mm) crystal analyzers of Si(111) and Ge (331) were chosen for the detection of the Lγ_3 (6341.5 eV) and the Lα_1 (4839 eV) emission lines, respectively.[22] The sample, the analyzer crystal, and the photon detector (Pilatus 100K) were arranged according to vertical Rowland geometry. The energy resolution (incident convoluted with emitted) was about 1.1 eV at 69° for Si(111) and 1.0 eV at 80.7° for Ge (331) . We used an in situ plug flow reactor[19] consisting of a 1 mm kapton tube with 0.02 mm wall thickness and an air heater. The spectra at Ce L_3 edge were collected for 20−60 min and at Ce L_1 edge for 30−180 min. The possibility of damage induced by X-ray irradiation for each samples was carefully analyzed, and when it was necessary the position of the beam on the sample was changed periodically moving to the fresh spot. In contrast to our previous observations[16] for ceria nanopowders measured in situ the X-ray induced irradiation damage was not observed. The explanations are the following: 1) the size of ceria nanoparticles in the present work were relatively big (8−100 nm), 2) we calcined all samples at 500 °C in air that helped to remove the traces precursors and OH groups from the surface, 3) ceria nanoparticles were promoted by Pt nanoparticles, which due to a spillover effect, helps keeping equilibrium concentration of oxygen species on ceria surface. The background subtraction and normalization of the spectra were performed by the Athena program from the IFEFFIT program package.[23] The principal component analysis and linear combination fit were performed using the Fitit software.[24] The spectra of the reference compounds CeO_2 (NIST), $Ce(NO_3)_3 \cdot 6H_2O$ (Aldrich), $CeAlO_3$, and $Ce_2Zr_2O_7$ were measured for comparison. $CeAlO_3$ and $Ce_2Zr_2O_7$ were prepared by solution combustion routes[25,26] followed by annealing in 5%H_2 in Ar at 800 °C for 24 h. The structure of these compounds was confirmed by XRD.

3. THEORETICAL METHODS

The electronic structure of the Ce-based compounds and the corresponding Ce L_1 and L_3 HERFD XANES spectra were simulated by means of the full-potential linearized augmented plane-wave approximation (FLAPW) implemented in the Wien2k program package.[27,28] The generalized gradient approximation within the Perdew, Burke, Ernzerhof exchange-correlation functional (GGA PBE)[29] was used for treatment of the exchange-correlation interaction. A correction for the self-interaction[30,31] was added for localized Ce 4f electrons with a U_{eff} value of 5 eV, as suggested in the work of Andersson et al.[32] Ce L_1 and L_3 edge spectra were well reproduced in the ground state approximation without a core hole. The plane wave basis set and the number of k-points in the reciprocal lattice were increased until variations in the calculated spectral shape were converged. Energy convergence in the self-consistent iteration procedure was better than 1 meV. The FLAPW approach enabled the accurate estimation of the core-level energies and atomic charges for the bulk compounds with high symmetry. To simulate spectra for the small ceria nanoparticles, we applied the real-space Green function within the muffin-tin approximation (GF-MTA), as implemented in the FDMNES code.[33] This approach is suitable for the simulation of small clusters with many nonequivalent positions and a lack of symmetry; however, it does not provide an accurate estimation of the core-level energies. According to the literature, a one-electron interpretation of Ce L_3 spectra is insufficient to describe the large 4f correlation energy.[34] However, the first part of the spectra (up to 15 eV above the adsorption edge) can be successfully simulated by this approximation.[17] The core-level energies along with Fermi level position, obtained from GGA +U FLAPW simulations, were used to determine the relative energy shift in the calculated XANES spectra, because this information was not available for all models. The spectra calculated according to the GF-MTA approach were energetically shifted to obtain the best agreement with the experimental data. The charge state of Ce was determined by Bader analysis[35,36] of the electron density, obtained with the FLAPW simulations for Ce reference compounds and model structures.

To validate the theoretical approaches, we first calculated Ce L_1 and L_3 HERFD XANES spectra for the CeO_2 and $Ce_2Zr_2O_7$ reference compounds (Table 1).

When a satisfactory agreement between the experimental and theoretical data was achieved, we applied the same input parameters to calculate the theoretical spectra of the model structures. We considered four model structures containing Ce^{3+}, calculated the theoretical Ce L_1 and L_3 HERFD XANES spectra, and compared the spectra with the experimental spectra of Ce^{3+} in ceria nanoparticles. In two model structures, cubic Ce_2O_3[41] and $Ce_{11}O_{20}$,[6] the Ce^{3+} ions were in the bulk.

dx.doi.org/10.1021/jp409571b | J. Phys. Chem. C XXXX, XXX, XXX−XXX

For Ce_2O_3 we calculated the spectra of both 6-fold coordinated nonequivalent sites and averaged them with the appropriate weights. The $Ce_{11}O_{20}$ structure consists of several cerium sites in a different oxidation state and in 7- or 8-fold coordination (Table 1). Two other structures contained Ce^{3+} on the surface: 1) The first structure described by Fronzi et al.[10] had cerium ions with a 4-fold oxygen coordination on the surface of fully reduced $CeO_2(111)$. We used the FLAPW approximation to relax the atomic positions in this structure until the forces the atoms were less than 0.03 eV/Å. 2) The other type of Ce^{3+} was on the surface of a $Ce_{21}O_{41}$ nanoparticle, as described by Migani et al.[11] This nanoparticle was produced from a stoichiometric $Ce_{21}O_{42}$ nanoparticle by removing of one oxygen atom (O_{2c}) from the small (100) facet and formation of two Ce^{3+} ions in a 6-fold coordination on the nanoparticle edge (Ce_{6c}). This structure was provided by Migani et al.[11] and was used without further optimization.

4. RESULTS AND DISCUSSION

4.1. Characterization of Microstructure. Figure 1 shows micrographs of ceria nanoparticles promoted with platinum. The shapes of the ceria particles are visible, and their size and orientation are as reported in the literature.[7] The platinum particles (indicated by arrows) are homogeneously distributed on the surface of the ceria. Statistical analysis (shown in the SI) shows that they are small (1.1 to 1.5 nm) and have a narrow size distribution. Table 2 gives the surface area, the concentration of platinum, and the size and the surface density of the platinum nanoparticles.

4.2. Characterization of Reactivity. The reactivity of ceria was analyzed by three methods: pulse experiments, XRD, and Ce L_1 and L_3 HERFD XANES spectroscopy. We compare the reactivity of ceria in each sample at 150 °C, as estimated from pulse experiments (Table 2), showing the OSC of ceria, the concentration of Ce^{3+} formed under reducing conditions, and the equivalent number of oxygen layers that can be reversibly extracted from the ceria surface. According to Pt L_3 XANES spectroscopy (Figure 2), upon CO-O_2 cycling at 150 °C not only the ceria but also the platinum change the oxidation state from metallic to partially oxidic. Considering this information, we extracted the parameters related to the reactivity of ceria (Table 2). The results demonstrate that the equivalent number of oxygen layers, which participate in the OSC of the ceria at 150 °C, is between 0.6 and 1.2, depends on the nature of ceria support but does not depend on the surface density of the platinum particles. In agreement with the literature,[7] the equivalent number is higher for ceria cubes with exposed (100) planes and rods with exposed (110) and (100) planes than for truncated polyhedra with exposed (111) and (100) planes.

XRD provided independent information about ceria reactivity, revealing the reversible changes in the lattice parameter (a) of ceria refined within cubic $Fm\bar{3}m$ structure for TO1 sample measured during CO-O_2 cycling at different temperatures (Figure 3). The lattice parameter of ceria increases with temperature. Moreover, under isothermal conditions, it increases further under reducing atmosphere (5% CO) due to formation of Ce^{3+} and decreases to the initial value under oxidizing conditions due to Ce^{3+} oxidation. At each temperature we estimated the concentration of Ce^{3+} formed, using the linear relation between the relative lattice expansion ($\Delta y/y$), and the Ce^{3+} concentration, using reference compounds: pure CeO_2[37] ($Fm\bar{3}m$, a = 5.4135 Å, 100% Ce^{4+}) and

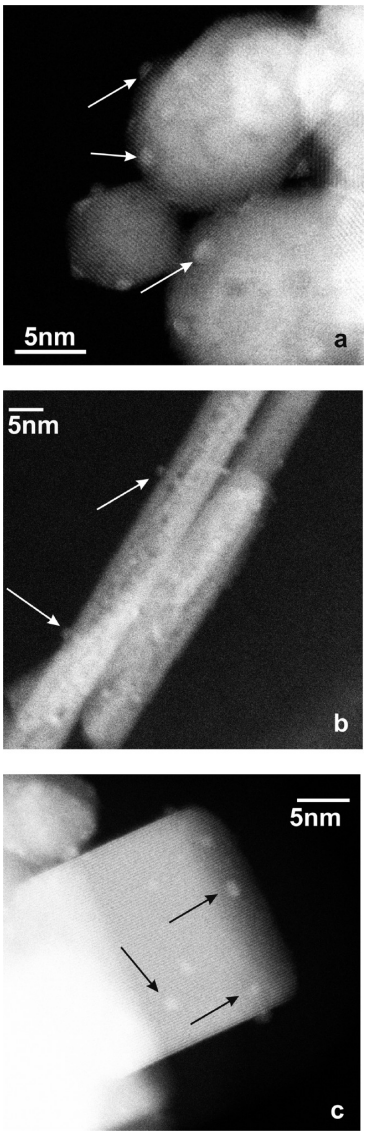

Figure 1. TEM images of TO2 (a), R1 (b), and C1 (c) samples. Arrows indicate at Pt nanoparticles.

$CeO_{1.68}$[6] ($Ia\bar{3}$, a = 11.1108 Å, 64% Ce^{3+}), where $y = a$ for the $Fm\bar{3}m$ structure and $y = 0.5 \times a$ only for the $Ia\bar{3}$ structure of $CeO_{1.68}$, which contains twice as many cerium atoms in the elemental cell than does $Fm\bar{3}m$ (Table 3).

The concentrations of Ce^{3+} in the TO1 sample, calculated from XRD data at 100 °C (4%) and 300 °C (7%), are lower than the concentrations obtained in the pulse experiments (8% at 150 °C). The discrepancy is due to the limitation of the linear relation approximation that was applied to analyze the XRD. This model might not be applicable when Ce^{3+} ions are formed mainly at the surface of ceria crystallites. Moreover, it does not take into account the local structure of oxygen vacancies.[14]

Finally, the reactivity of ceria was analyzed by X-ray absorption spectroscopy.[42] Figure 4 represents the experimental HERFD XANES Ce L_3 spectra, collected for R1 and TO2 under oxidizing (4% O_2) conditions at 150 °C and under reducing (5% CO) conditions at 50 to 240 °C. Under oxidizing conditions the spectra are very similar to those of CeO_2,[15,16] confirming the presence of Ce^{4+} ions with an 8-fold oxygen coordination[37] and a negligible concentration of Ce^{3+}. Under

dx.doi.org/10.1021/jp409571b | J. Phys. Chem. C XXXX, XXX, XXX−XXX

Table 2. Structure of the Samples: Sample Names, Shape of Ceria Nanoparticles, Specific Surface Area (S), Concentration of Platinum (C_{Pt}), Average Size of Platinum Nanoparticles (d_{Pt}) with Standard Deviation (in Brackets), Surface Density of Platinum Nanoparticles (C_{NP}), OSC of Ceria Surface Measured at 150 °C, Corresponding Concentration of Ce^{3+} Ions, and Number of Removed Oxygen Layers (L[O])

sample	shape	S, $m^2 \cdot g^{-1}$	C_{Pt}, wt%	d_{Pt}, nm	C_{NP}, nm^{-2}	CeO_2 OSC, $\mu mol[O] \cdot m^{-2}$	Ce^{3+}, %	L[O]
TO1		60	2.0	1.5 (0.3)	0.008	3.6	8	0.6
TO2	truncated	85	1.5	1.2 (0.2)	0.009	3.7	11	0.6
TO3	octahedra	85	1.0	1.3 (0.2)	0.005	3.4	10	0.55
TO4		85	0.5	1.1 (0.2)	0.004	3.4	10	0.55
R1	rods	70	1.26	1.5 (0.4)	0.003	6.0	14	1.2
C1	cubes	14	0.24	1.2 (0.3)	0.006	4.8	2	0.8

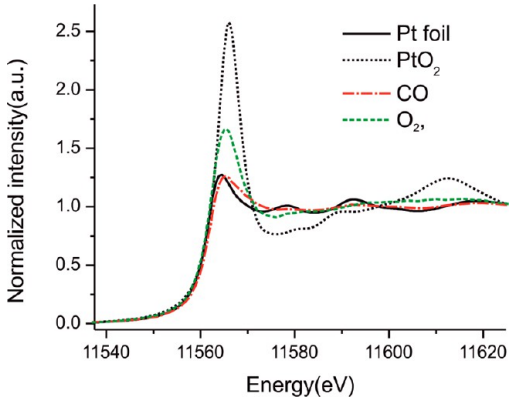

Figure 2. The Pt L_3 edge XANES spectra of TO1 sample in 5% CO and 4% O_2 at 150 °C were measured in situ and compared with the Pt and PtO_2 reference samples.

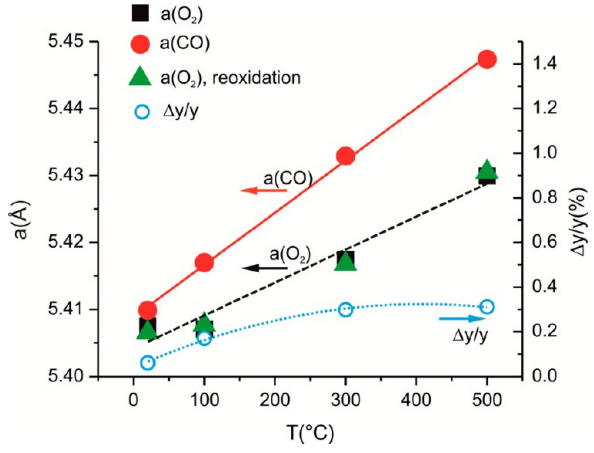

Figure 3. The unit cell parameter of ceria (a) for TO1 in 2% O_2 and 5% CO as a function of temperature and the relative lattice expansion ($\Delta y/y$) in 5% CO.

Table 3. Concentration of Ce^{3+} at Different Temperatures in 5% CO, Estimated from in Situ XRD Data

sample	temp, °C	$\Delta y/y$, %	Ce^{3+}, %
CeO_2[a]	25	0	0
$CeO_{1.68}$[a]	25	2.8	64
TO1	25	0.06	1.4
TO1	100	0.17	4
TO1	300	0.30	7
TO1	400	0.31	7

[a]Reference compounds.

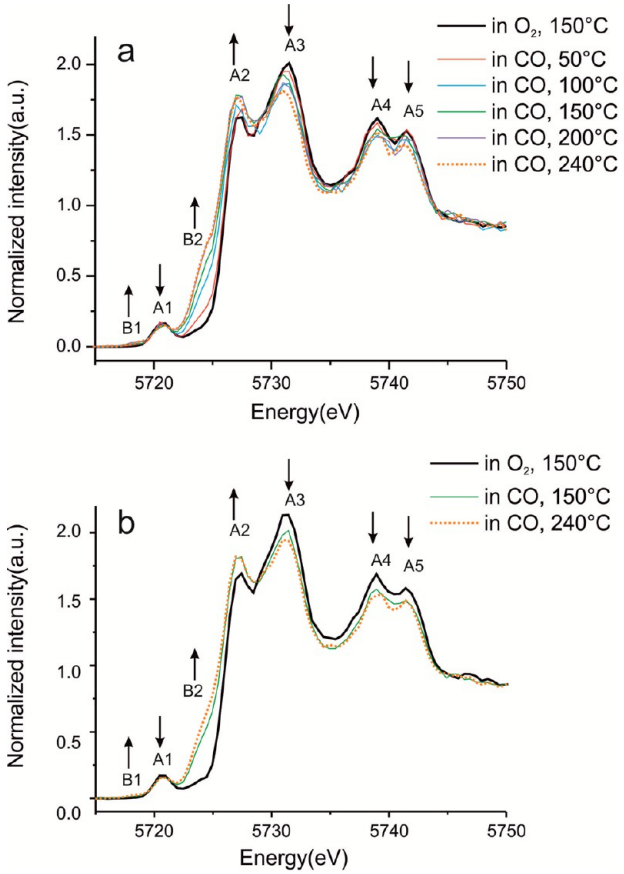

Figure 4. In situ Ce L_3 HERFD XANES spectra of R1 (a) and TO2 (b) samples under oxidizing (4% O_2, 150 °C) and reducing (5% CO, 50−240 °C) conditions. Arrows indicate the direction of change under reducing conditions.

reducing conditions almost all the spectral features corresponding to CeO_2 (A1-A5) are less intense, except for A2. The new features B1 (pre-edge) and B2 already appear at 50 °C and continue to increase in intensity up to 240 °C when the reduction process slows down indicating that the maximum LT OSC has been reached. By means of PCA we determined that the spectra can be presented as a linear combination of two independent components. The first component was fixed as Ce^{4+} in the CeO_2 structure, and the second component was assigned to Ce^{3+} with an unknown local coordination. The spectra of the second component were obtained assuming that the concentrations of Ce^{3+} in R1 and TO2 samples are equal to 14% and 11%, respectively, as determined independently by OSC tests (Table 2). The second component spectrum is very

dx.doi.org/10.1021/jp409571b | J. Phys. Chem. C XXXX, XXX, XXX−XXX

similar in both samples (Figure 5a). The concentration of Ce^{3+} depends on the temperature (Table 4).

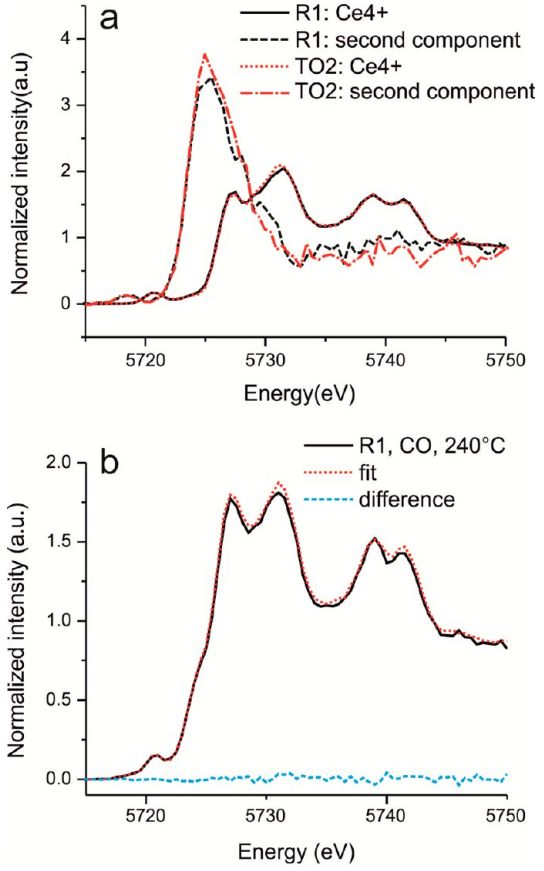

Figure 5. Ce L_3 HERFD XANES spectra of (a) the first (Ce^{4+}) and second (Ce^{3+}) spectral component of R1 and TO2 samples and (b) an example of a linear combination fit of the experimental spectrum (R1 in 5%CO at 240 °C).

Table 4. Concentrations of Ce^{3+} under Different Reaction Conditions in R1 and TO2 Samples, Estimated from Ce L_3 HERFD XANES

experimental conditions	Ce^{3+} in R1 samples, %	Ce^{3+} in TO2 sample, %
5% CO, 50 °C	2.6	-
5% CO, 100 °C	11	-
5% CO, 150 °C	14[a]	11[a]
5% CO, 200 °C	17	-
5% CO, 240 °C	18	15

[a]Estimated from OSC tests.

Figure 5b shows an example of the excellent linear combination fit and the difference spectrum. We also measured Ce L_1 edge spectra for R1 and TO2 samples in situ in 5% CO and 4% O_2 and performed a linear combination analysis to extract the components corresponding to the spectra of Ce^{4+} ions and the newly found cerium species (Figure 6). We compare the Ce L_3 and L_1 HERFD XANES spectra of the second component with the experimental spectra of the reference compounds of Ce^{3+} with a known local coordination (Figure 8). Two features are particular to the Ce L_3 spectra (Figure 7a): 1) The position of the main Ce L_3 edge (B2) of the new component is systematically shifted toward lower energies by 1−2 eV compared to the reference samples, except

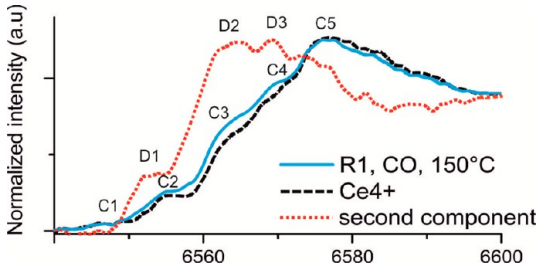

Figure 6. Ce L_1 HERFD XANES spectrum of R1 in 5%CO at 150 °C and the corresponding first (Ce^{4+}) and second (Ce^{3+}) spectral component.

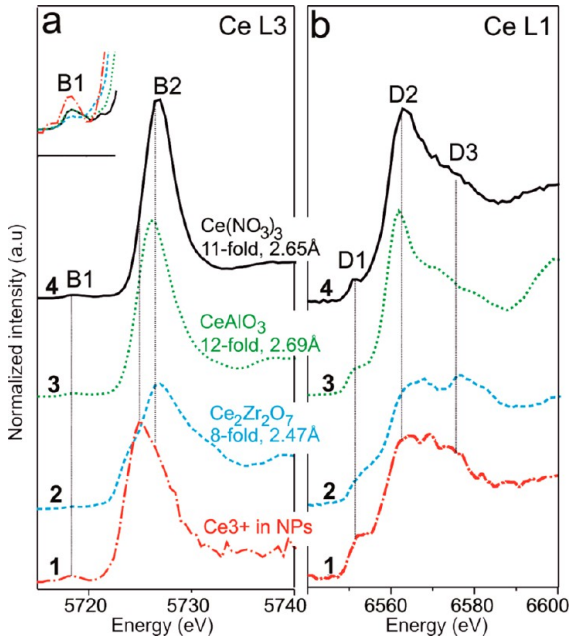

Figure 7. Comparison of (a) Ce L_3 and (b) Ce L_1 HERFD XANES spectra of Ce^{3+} ions in CeO_2 nanoparticles (spectrum 1) with the spectra of Ce^{3+} ions in $Ce_2Zr_2O_7$ (2), $CeAlO_3$ (3), $Ce(NO_3)_3{\cdot}6H_2O$ (4). Inset (a): pre-edge B1 region of Ce L_3. Coordination of Ce^{3+} in the first shell and corresponding Ce−O distances are indicated above each plot.

for $Ce_2Zr_2O_7$, which shows a similar edge position but a broader feature. 2) The position of the pre-edge B1 is at the same energy as for the reference compounds and for the second component spectrum. This enables the assignment of the newly found component to a Ce^{3+} species, as expected. The main Ce L_3 edge is typically assigned to the $2p_{3/2}$ to $5d_{5/2}$ transition and the pre-edge to the $2p_{3/2}$ to 4f transition.[15,43] Since 4f orbitals have a local character, they do not participate directly in chemical bonding with the ligands. Therefore, their position (B1 feature) depends mainly on the number of electrons in the f orbitals. In contrast, the d orbitals of cerium have a more favorable geometry for interaction with orbitals of the oxygen ligands and can form different states resulting in the observed shift in the L_3 edge (d-band). This shift can be used as a fingerprint of the electronic structure of Ce^{3+} ions, which form in ceria nanoparticles. The Ce L_1 spectra (Figure 7b) originate from the 2s to 6p transition. The intensity of the D2 and D3 features changes systematically with the local coordination around the Ce^{3+} ion: The D2 feature is more intense for higher Ce−O coordination numbers and longer Ce−O distances.

dx.doi.org/10.1021/jp409571b | J. Phys. Chem. C XXXX, XXX, XXX−XXX

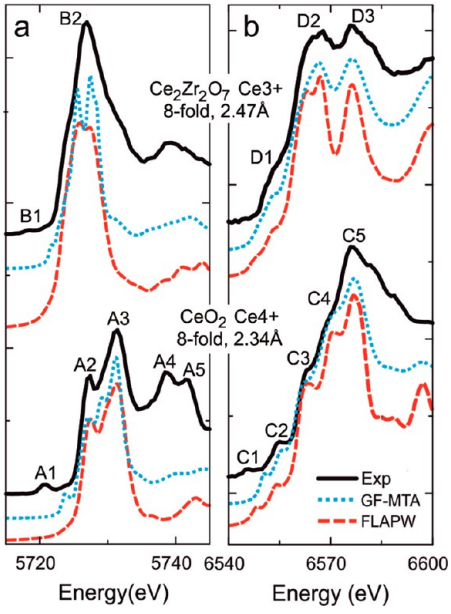

Figure 8. Comparison of experimental (a) Ce L_3 and (b) Ce L_1 HERFD XANES spectra of the CeO_2 and $Ce_2Zr_2O_7$ reference samples (solid curves) and the corresponding spectra simulated by GF-MTA (dotted curves) and FLAPW (dashed curves) approaches. Oxidation state of Ce, coordination number in the first shell and corresponding Ce−O distances are indicated above each plot.

4.3. XAS Analysis: Comparison to Theoretical Simulations. The Ce L_3 and L_1 spectra of Ce^{4+} in CeO_2 and Ce^{3+} in $Ce_2Zr_2O_7$ reference compounds are simulated by the FLAPW and GF-MTA approximations (Figure 8). The simulated spectra in both approaches qualitatively reproduce all the features except for the pre-edge features (A1, B1, C1) and the high-energy part of the Ce L_3 XANES spectra of CeO_2 (A4 and A5 peaks), which originates from multielectron excitations.[17] The Ce L_3 and L_1 absorption spectra of Ce^{3+} ions show a systematic shift of edge position toward lower energy compared to that of Ce^{4+}.

The experimental Ce L_3 and L_1 spectra of the newly determined Ce^{3+} species (a and b) are compared with the spectra of model structures simulated by FLAPW (c and d) and GF-MTA (e and f) (Figure 9; Table 1). Conclusions: 1) The positions of the Ce L_3 and L_1 edges of $Ce_{11}O_{20}$, calculated by FLAPW, indicate that 8-fold sites having longer Ce−O distances of 2.51 Å (spectrum 1 in Figure 9) correspond to Ce^{3+}, while 7-fold coordinated sites (spectrum 3) with a shorter Ce−O distances of 2.33 Å and an oxygen vacancy in the first coordination shell, correspond to Ce^{4+}. This confirms a general trend, typical of oxygen-deficit ceria surfaces: Oxygen vacancies move away from the first coordination shell of Ce^{3+} to that of Ce^{4+}.[11,13] Our simulations indicate that this trend is also valid for the bulk structures. 2) The simulations demonstrate that the experimental spectra of Ce^{3+}, which forms in the ceria nanoparticles, are more similar to those of the 8-fold site in the $Ce_{11}O_{20}$ structure (spectrum 1) than to the 6-fold coordinated Ce^{3+} spectra in the Ce_2O_3 with mean Ce−O

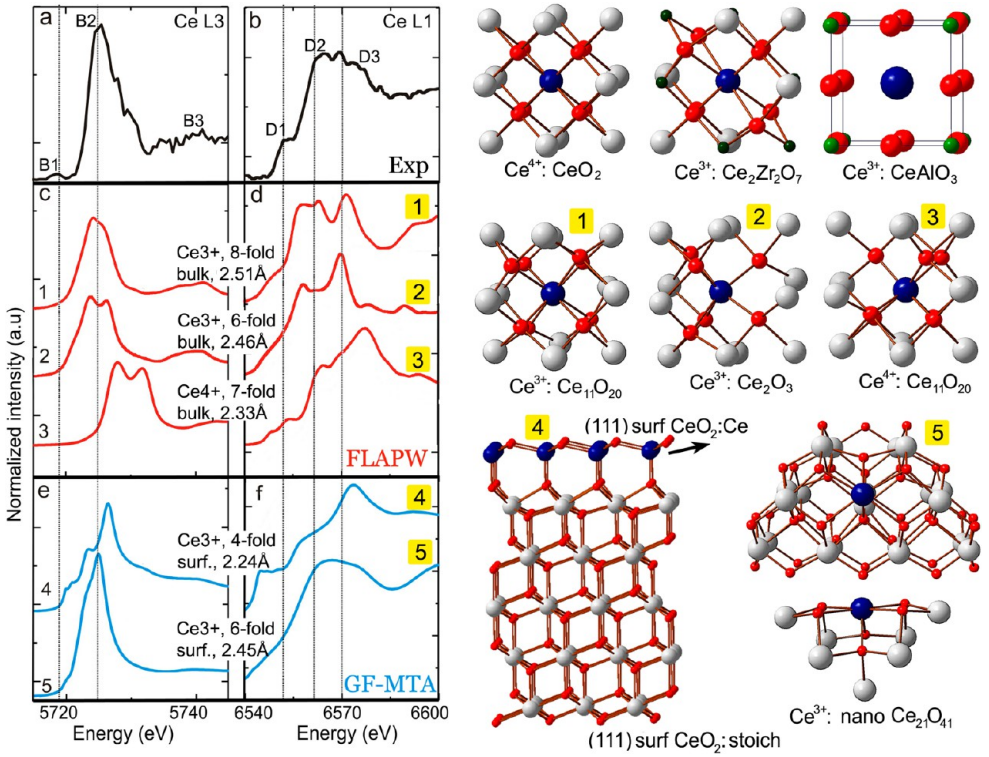

Figure 9. Left: Experimental (a) Ce L_3 and (b) Ce L_1 HERFD XANES spectra of Ce^{3+} species taken from R1 sample compared to simulated spectra of model structures by FLAPW (c and d) and GF-MTA (e and f). The spectrum (1) corresponds to Ce^{3+} site in $Ce_{11}O_{20}$, (2) corresponds Ce^{3+} site in Ce_2O_3, (3) corresponds to Ce^{4+} site in $Ce_{11}O_{20}$, (4) corresponds cerium site on reduced CeO_2(111):Ce surface, and (5) corresponds to Ce^{3+} site in the $Ce_{21}O_{41}$ nanoparticle. Oxidation state of Ce, coordination number in the first shell and corresponding Ce−O distances are indicated above each plot. Right: local coordination of Ce in the reference structures: blue spheres correspond to Ce atoms used for simulations, white spheres to other Ce atoms, red spheres to O, black spheres to Zr, and green spheres to Al.

dx.doi.org/10.1021/jp409571b | J. Phys. Chem. C XXXX, XXX, XXX−XXX

distance of 2.46 Å (spectrum 2). A comparison of the relative intensity of the D2 and D3 features on the L_1 edge and the shape of the L_3 main edge support this conclusion. 3) The structure of the 4-fold coordinated site on the $CeO_2(111)$:Ce surface with mean Ce−O distance of 2.24 Å (spectrum 4) does not correspond well to the experimental spectra. 4) The spectra of 6-fold coordinated Ce^{3+} sites on the surface of partially reduced $Ce_{21}O_{41}$ nanoparticles with mean Ce−O distance of 2.45 Å (spectrum 5) are in good agreement with the experimental data.

Overall, a comparison of theoretical and experimental data lead to the conclusion that the Ce L_1 and L_3 HERFD XANES spectra are less sensitive with regards to the number of oxygen neighbors in the first coordination shell of Ce^{3+} than with regard to the corresponding Ce−O coordination distance (additional information is given in the SI). Ce^{3+} in the bulk of $Ce_{11}O_{20}$ and on the surface of $Ce_{21}O_{41}$ nanoparticle (Table 1) has a different symmetry but similar spectral features. In both structures, the mean Ce−O distance in the first coordination shell (2.51 Å and 2.45 Å, respectively) increases (4−7%) compared to pure CeO_2 (2.34 Å), and the Ce−Ce distance in the second coordination shell is almost unchanged (3.83−3.86 Å vs 3.83 Å in CeO_2). Similar coordination distances are also characteristic of Ce^{3+} in the $Ce_2Zr_2O_7$ reference structure (2.47 Å for Ce−O and 3.78 Å for Ce−Ce), which also have similar Ce L_1 and L_3 X-ray absorption spectra. Other reference structures demonstrate different structural trends: For $CeAlO_3$ and $Ce(NO_3)_3{\cdot}6H_2O$ the Ce−O distances are longer (2.69 Å and 2.65 Å vs 2.34 Å in CeO_2) and the second coordination shell is at a much shorter distance (3.30 Å and 3.15 Å vs 3.83 Å in CeO_2), whereas for Ce_2O_3 both the Ce−O (2.46 Å) and Ce−Ce (4.08 Å) coordination distances are longer, and for $CeO_2(111)$:Ce the Ce−O distances (3.24 Å) are shorter and Ce−Ce distances (3.90 Å) are slightly longer.

These results explain why the PCA analysis revealed only two components in the Ce L_1 and L_3 HERFD XANES spectra of ceria nanoparticles under reducing conditions. Formation of Ce^{3+} species with similar coordination distances and various local symmetry (especially on the surface) is possible, but we cannot distinguish among them by means of Ce L_1 and L_3 HERFD XANES. At the same time, based on the coordination distances calculated by Ce L_1 and L_3 HERFD XANES, we exclude the formation of a Ce_2O_3-like structure and 4-fold coordinated Ce^{3+} species with a shorter Ce−O distance (3.24 Å). The most probable Ce^{3+} species in the ceria nanoparticles have elongated Ce−O and an almost unchanged Ce−Ce distance compared to stoichiometric CeO_2. The neighboring cerium atoms in the second coordination shell of Ce^{3+} probably have shorter Ce−O coordination distances and must have a 4+ charge as in $Ce_{11}O_{20}$.

CONCLUSIONS

In CO under reducing conditions at 50−240 °C oxygen atoms are extracted mainly from the surface of CeO_2 nanoparticles. This is accompanied by considerable expansion of the lattice of CeO_2, as revealed by XRD. Experimental data demonstrate that the electronic structure of Ce^{3+} species in ceria nanoparticles have an f^1 configuration, similar to that of stable reference compounds ($CeAlO_3$, $Ce(NO_3)_3{\cdot}6H_2O$, $Ce_2Zr_2O_7$) but a different d-band structure. Using reference compounds we demonstrated that Ce L_1 and L_3 XAS spectra can be successfully simulated using ground state approximation and two alternative theoretical approaches, namely FLAPW and GF-MTA. The local structure of Ce^{3+} ions probably corresponds to a 6- and a 7-fold coordination on the surface and an 8-fold coordination in the bulk. All the Ce^{3+} species are characterized by elongated Ce−O distances in the first coordination shell compared to stoichiometric CeO_2 and almost the same Ce−Ce distance in the second coordination shell.

ASSOCIATED CONTENT

Supporting Information

Synthesis of shaped ceria nanoparticles; deposition of platinum nanoparticles by incipient wetness impregnation; transmission electron microscopy; Ce L_1 XANES simulations: effect of the core hole; Ce L_1 and L_3 XANES simulations: effect of geometric structure. This material is available free of charge via the Internet at http://pubs.acs.org.

AUTHOR INFORMATION

Corresponding Authors

*Phone: +41 56 310 5805. E-mail: olga.safonova@psi.ch.

*Phone: +41 44 632 5542. E-mail: jeroen.vanbokhoven@chem.ethz.ch.

Notes

The authors declare no competing financial interest.

ACKNOWLEDGMENTS

We thank Prof. G. Vyassilov for providing the structure of the optimized $Ce_{21}O_{41}$ cluster. We thank Dr. T. Baidya and Dr. E. Pomjakushina for synthesizing the reference compounds and Dr. F. Krumeich for the TEM measurements. We are grateful to SLS and SNBL for beamtime and technical support and the UGINFO computer center of the Southern Federal University, Rostov-on-Don, for the computer time and Dr. V. N. Datsyuk for assistance. A.A.G., M.A.S., and A.V.S. would like to thank the Russian Ministry of Education and Science for financial support (Project #11.519.11.2039).

REFERENCES

(1) Trovarelli, A. *Catalysis by Ceria and Related Materials*; Imperial College Press: 2002.

(2) Kašpar, J.; Fornasiero, P.; Graziani, M. Use of CeO_2-Based Oxides in the Three-Way Catalysis. *Catal. Today* **1999**, *50*, 285−298.

(3) Steele, B. C. H.; Heinzel, A. Materials for Fuel-Cell Technologies. *Nature* **2001**, *414*, 345−352.

(4) Kosinski, M. R.; Baker, R. T. Preparation and Property−Performance Relationships in Samarium-Doped Ceria Nanopowders for Solid Oxide Fuel Cell Electrolytes. *J. Power Sources* **2011**, *196*, 2498−2512.

(5) Chueh, W. C.; Falter, C.; Abbott, M.; Scipio, D.; Furler, P.; Haile, S. M.; Steinfeld, A. High-Flux Solar-Driven Thermochemical Dissociation of CO_2 and H_2O Using Nonstoichiometric Ceria. *Science* **2010**, *330*, 1797−1801.

(6) Kümmerle, E. A.; Heger, G. The Structures of C−$Ce_2O_{3+\delta}$, Ce_7O_{12}, and $Ce_{11}O_{20}$. *J. Solid State Chem.* **1999**, *147*, 485−500.

(7) Mai, H.-X.; Sun, L.-D.; Zhang, Y.-W.; Si, R.; Feng, W.; Zhang, H.-P.; Liu, H.-C.; Yan, C.-H. Shape-Selective Synthesis and Oxygen Storage Behavior of Ceria Nanopolyhedra, Nanorods, and Nanocubes. *J. Phys. Chem. B* **2005**, *109*, 24380−24385.

(8) Mikulová, J.; Barbier, J., Jr.; Rossignol, S.; Mesnard, D.; Duprez, D.; Kappenstein, C. Wet Air Oxidation of Acetic Acid Over Platinum Catalysts Supported on Cerium-Based Materials: Influence of Metal and Oxide Crystallite Size. *J. Catal.* **2007**, *251*, 172−181.

(9) Herschend, B.; Baudin, M.; Hermansson, K. Electronic Structure of the CeO_2(1 1 0) Surface Oxygen Vacancy. *Surf. Sci.* **2005**, *599*, 173−186.

(10) Fronzi, M.; Soon, A.; Delley, B.; Traversa, E.; Stampfl, C. Stability and Morphology of Cerium Oxide Surfaces in an Oxidizing Environment: A First-Principles Investigation. *J. Chem. Phys.* **2009**, *131*, 104701.
(11) Migani, A.; Vayssilov, G. N.; Bromley, S. T.; Illas, F.; Neyman, K. M. Dramatic Reduction of the Oxygen Vacancy Formation Energy in Ceria Particles: A Possible Key to Their Remarkable Reactivity at the Nanoscale. *J. Mater. Chem.* **2010**, *20*, 10535−10546.
(12) Vayssilov, G. N.; Lykhach, Y.; Migani, A.; Staudt, T.; Petrova, G. P.; Tsud, N.; Skála, T.; Bruix, A.; Illas, F.; Prince, K. C.; et al. Support Nanostructure Boosts Oxygen Transfer to Catalytically Active Platinum Nanoparticles. *Nat. Mater.* **2011**, *10*, 310−315.
(13) Jerratsch, J.-F.; Shao, X.; Nilius, N.; Freund, H.-J.; Popa, C.; Ganduglia-Pirovano, M. V.; Burow, A. M.; Sauer, J. Electron Localization in Defective Ceria Films: A Study with Scanning-Tunneling Microscopy and Density-Functional Theory. *Phys. Rev. Lett.* **2011**, *106*, 246801.
(14) Kossoy, A.; Frenkel, A. I.; Feldman, Y.; Wachtel, E.; Milner, A.; Lubomirsky, I. The Origin of Elastic Anomalies in Thin Films of Oxygen Deficient Ceria, CeO_{2-x}. *Solid State Ionics* **2010**, *181*, 1473−1477.
(15) Kvashnina, K. O.; Butorin, S. M.; Glatzel, P. Direct Study of the F-Electron Configuration in Lanthanide Systems. *J. Anal. At. Spectrom.* **2011**, *26*, 1265−1272.
(16) Paun, C.; Safonova, O. V.; Szlachetko, J.; Abdala, P. M.; Nachtegaal, M.; Sa, J.; Kleymenov, E.; Cervellino, A.; Krumeich, F.; van Bokhoven, J. A. Polyhedral CeO_2 Nanoparticles: Size-Dependent Geometrical and Electronic Structure. *J. Phys. Chem. C* **2012**, *116*, 7312−7317.
(17) Soldatov, A. V.; Ivanchenko, T. S.; Della Longa, S.; Kotani, A.; Iwamoto, Y.; Bianconi, A. Crystal-Structure Effects in the Ce L_3-Edge X-Ray-Absorption Spectrum of CeO_2: Multiple-Scattering Resonances and Many-Body Final States. *Phys. Rev. B* **1994**, *50*, 5074−5080.
(18) Abdala, P. M.; Safonova, O. V.; Wiker, G.; van Beek, W.; Emerich, H.; van Bokhoven, J. A.; Sa, J.; Szlachetko, J.; Nachtegaal, M. Scientific Opportunities for Heterogeneous Catalysis Research at the SuperXAS and SNBL Beam Lines. *Chimia* **2012**, *66*, 699−705.
(19) Van Beek, W.; Safonova, O. V.; Wiker, G.; Emerich, H. SNBL, a Dedicated Beamline for Combined in Situ X-Ray Diffraction, X-Ray Absorption and Raman Scattering Experiments. *Phase Transitions* **2011**, *84*, 726−732.
(20) Madier, Y.; Descorme, C.; Le Govic, A. M.; Duprez, D. Oxygen Mobility in CeO_2 and $Ce_xZr_{(1-x)}O_2$ Compounds: Study by CO Transient Oxidation and $^{18}O/^{16}O$ Isotopic Exchange. *J. Phys. Chem. B* **1999**, *103*, 10999−11006.
(21) Rodriguez-Carvajal, J. Recent Development of the Program FULLPROF. *Commission Powder Diffr. IUCr Newsl. 26*, 12−19.
(22) Kleymenov, E.; van Bokhoven, J. A.; David, C.; Glatzel, P.; Janousch, M.; Alonso-Mori, R.; Studer, M.; Willimann, M.; Bergamaschi, A.; Henrich, B.; et al. Five-Element Johann-Type X-Ray Emission Spectrometer with a Single-Photon-Counting Pixel Detector. *Rev. Sci. Instrum.* **2011**, *82*, 065107.
(23) Newville, M. *IFEFFIT*: Interactive XAFS Analysis and *FEFF* Fitting. *J. Synchrotron Radiat.* **2001**, *8*, 322−324.
(24) Smolentsev, G.; Soldatov, A. V. FitIt: New Software to Extract Structural Information on the Basis of XANES Fitting. *Comput. Mater. Sci.* **2007**, *39*, 569−574.
(25) Aruna, S. T.; Kini, N. S.; Shetty, S.; Rajam, K. S. Synthesis of Nanocrystalline CeAlO3 by Solution-Combustion Route. *Mater. Chem. Phys.* **2010**, *119*, 485−489.
(26) Baidya, T.; Hegde, M. S.; Gopalakrishnan, J. Oxygen-Release/Storage Properties of $Ce_{0.5}M_{0.5}O_2$ (M = Zr, Hf) Oxides: Interplay of Crystal Chemistry and Electronic Structure. *J. Phys. Chem. B* **2007**, *111*, 5149−5154.
(27) Blaha, P.; Schwarz, K.; Sorantin, P.; Trickey, S. B. Full-Potential, Linearized Augmented Plane Wave Programs for Crystalline Systems. *Comput. Phys. Commun.* **1990**, *59*, 399−415.
(28) Blaha, P.; Schwartz, K.; Madsen, G. H. K.; Kvasnicka, D.; Luitz, J. *Wien2K. An Augmented PlaneWave + Local Orbitals Program for Calculating Crystal Properties*; revised ed. WIEN2k 13.1 (Release 06/26/2013); Techn. Universitat. Wien, Institut fur Physikalische und Theoretische Chemie Getreidemarkt: 9/156 A-1060Wien/Austria, 2001.
(29) Perdew, J. P.; Burke, K.; Ernzerhof, M. Generalized Gradient Approximation Made Simple. *Phys. Rev. Lett.* **1996**, *77*, 3865−3868.
(30) Anisimov, V. I.; Solovyev, I. V.; Korotin, M. A.; Czyżyk, M. T.; Sawatzky, G. A. Density-Functional Theory and NiO Photoemission Spectra. *Phys. Rev. B* **1993**, *48*, 16929−16934.
(31) Madsen, G. K. H.; Novák, P. Charge Order in Magnetite. An LDA+U Study. *EPL Europhys. Lett.* **2005**, *69*, 777.
(32) Andersson, D. A.; Simak, S. I.; Johansson, B.; Abrikosov, I. A.; Skorodumova, N. V. Modeling of CeO_2, Ce_2O_3, and CeO_{2-x} in the LDA+U Formalism. *Phys. Rev. B* **2007**, *75*, 035109.
(33) Bunău, O.; Joly, Y. Self-Consistent Aspects of X-Ray Absorption Calculations. *J. Phys.: Condens. Matter* **2009**, *21*, 345501.
(34) Bianconi, A.; Marcelli, A.; Dexpert, H.; Karnatak, R.; Kotani, A.; Jo, T.; Petiau, J. Specific Intermediate-Valence State of Insulating 4f Compounds Detected by L_3 X-Ray Absorption. *Phys. Rev. B* **1987**, *35*, 806−812.
(35) Bader, R. F. W. *Atoms in Molecules: A Quantum Theory*; Clarendon Press: Oxford; New York, 1990.
(36) Bader, R. F. W. A Quantum Theory of Molecular Structure and Its Applications. *Chem. Rev.* **1991**, *91*, 893−928.
(37) Singh, P.; Hegde, M. S. $Ce_{1-x}Ru_xO_{2-\delta}$ (x=0.05, 0.10): A New High Oxygen Storage Material and Pt, Pd-Free Three-Way Catalyst. *Chem. Mater.* **2009**, *21*, 3337−3345.
(38) Vasylechko, L.; Senyshyn, A.; Trots, D.; Niewa, R.; Schnelle, W.; Knapp, M. $CeAlO_3$ and $Ce_{1-x}R_xAlO_3$ (R=La, Nd) Solid Solutions: Crystal Structure, Thermal Expansion and Phase Transitions. *J. Solid State Chem.* **2007**, *180*, 1277−1290.
(39) Milinski, N.; Ribar, B.; Sataric, M. Pentaaquatrinitratocerium-(III) Monohydrate, $Ce(H_2O)_5(NO_3)_3*H_2O$. *Cryst. Struct. Commun.* **1980**, *9*, 473−477.
(40) Achary, S. N.; Sali, S. K.; Kulkarni, N. K.; Krishna, P. S. R.; Shinde, A. B.; Tyagi, A. K. Intercalation/Deintercalation of Oxygen: A Sequential Evolution of Phases in Ce_2O_3/CeO_2−ZrO_2 Pyrochlores. *Chem. Mater.* **2009**, *21*, 5848−5859.
(41) Hirosaki, N.; Ogata, S.; Kocer, C. Ab Initio Calculation of the Crystal Structure of the Lanthanide Ln_2O_3 Sesquioxides. *J. Alloys Compd.* **2003**, *351*, 31−34.
(42) Bordiga, S.; Groppo, E.; Agostini, G.; van Bokhoven, J. A.; Lamberti, C. Reactivity of Surface Species in Heterogeneous Catalysts Probed by In Situ X-Ray Absorption Techniques. *Chem. Rev.* **2013**, *113*, 1736−1850.
(43) Kotani, A.; Kvashnina, K. O.; Butorin, S. M.; Glatzel, P. A New Method of Directly Determining the Core−Hole Effect in the Ce L_3 XAS of Mixed Valence Ce Compounds—An Application of Resonant X-Ray Emission Spectroscopy. *J. Electron Spectrosc. Relat. Phenom.* **2011**, *184*, 210−215.